The TESS-Keck Survey. XII. A Dense 1.8 R Ultra-short-period Planet Possibly Clinging to a High-mean-molecular-weight Atmosphere after the First Gigayear

Rubenzahl, Ryan A.; Dai, Fei; Howard, Andrew W.; Lissauer, Jack J.; Van Zandt, Judah; Beard, Corey; Giacalone, Steven; Murphy, Joseph M. Akana; Chontos, Ashley; Lubin, Jack; Brinkman, Casey L.; Tyler, Dakotah; MacDougall, Mason G.; Rice, Malena; Dalba, Paul A.; Mayo, Andrew W.; Weiss, Lauren M.; Polanski, Alex S.; Blunt, Sarah; Yee, Samuel W.

Link to publication on Research at Birmingham portal

The TESS-Keck Survey. XII. A Dense 1.8 $R_\oplus$ Ultra-short-period Planet Possibly Clinging to a High-mean-molecular-weight Atmosphere after the First Gigayear

Ryan A. Rubenzahl[1,26], Fei Dai[1,2,27], Andrew W. Howard[1], Jack J. Lissauer[3], Judah Van Zandt[4], Corey Beard[5,28],
Steven Giacalone[1,29], Joseph M. Akana Murphy[6,26], Ashley Chontos[7,8,30], Jack Lubin[5], Casey L. Brinkman[8],
Dakotah Tyler[4], Mason G. MacDougall[4], Malena Rice[9], Paul A. Dalba[6], Andrew W. Mayo[10], Lauren M. Weiss[11],
Alex S. Polanski[12], Sarah Blunt[1,13], Samuel W. Yee[7,14], Michelle L. Hill[15], Isabel Angelo[4], Emma V. Turtelboom[10],
Rae Holcomb[5], Aida Behmard[16], Daria Pidhorodetska[15], Natalie M. Batalha[6], Ian J. M. Crossfield[12],
Courtney Dressing[10], Benjamin Fulton[17], Daniel Huber[8,18], Howard Isaacson[10,19], Stephen R. Kane[15],
Erik A. Petigura[4], Paul Robertson[5], Nicholas Scarsdale[6], Teo Mocnik[20], Tara Fetherolf[15,21], Luca Malavolta[22,23],
Annelies Mortier[24], Aldo Fiorenzano[25], and Marco Pedani[25]

[1] Department of Astronomy, California Institute of Technology, Pasadena, CA 91125, USA
[2] Division of Geological and Planetary Science, California Institute of Technology, Pasadena, CA 91125, USA
[3] Space Science & Astrobiology Division, MS 245-3, NASA Ames Research Center, Moffett Field, CA 94035, USA
[4] Department of Physics & Astronomy, University of California Los Angeles, Los Angeles, CA 90095, USA
[5] Department of Physics & Astronomy, University of California Irvine, Irvine, CA 92697, USA
[6] Department of Astronomy and Astrophysics, University of California, Santa Cruz, CA 95064, USA
[7] Department of Astrophysical Sciences, Princeton University, 4 Ivy Lane, Princeton, NJ 08540, USA
[8] Institute for Astronomy, University of Hawai'i, Honolulu, HI 96822, USA
[9] Department of Astronomy, Yale University, New Haven, CT 06511, USA
[10] Department of Astronomy, University of California Berkeley, Berkeley, CA 94720, USA
[11] Department of Physics and Astronomy, University of Notre Dame, Notre Dame, IN 46556, USA
[12] Department of Physics and Astronomy, University of Kansas, Lawrence, KS 66045, USA
[13] CIERA, Northwestern University, Evanston IL 60201, USA
[14] Center for Astrophysics | Harvard & Smithsonian, 60 Garden Street, Cambridge, MA 02138, USA
[15] Department of Earth and Planetary Sciences, University of California, Riverside, CA 92521, USA
[16] Department of Astrophysics, American Museum of Natural History, 200 Central Park West, Manhattan, NY 10024, USA
[17] NASA Exoplanet Science Institute/Caltech-IPAC, MC 314-6, 1200 E. California Boulevard, Pasadena, CA 91125, USA
[18] Sydney Institute for Astronomy (SIfA), School of Physics, University of Sydney, NSW 2006, Australia
[19] Centre for Astrophysics, University of Southern Queensland, Toowoomba, QLD, Australia
[20] Gemini Observatory/NSF's NOIRLab, 670 N. A'ohoku Place, Hilo, HI 96720, USA
[21] Department of Physics, California State University, San Marcos, CA 92096, USA
[22] Dipartimento di Fisica e Astronomia "Galileo Galilei," Universitá di Padova, Vicolo dell'Osservatorio 3, IT-35122, Padova, Italy
[23] INAF—Osservatorio Astronomico di Padova, Vicolo dell'Osservatorio 5, IT-35122, Padova, Italy
[24] School of Physics and Astronomy, University of Birmingham, Edgbaston, Birmingham B15 2TT, UK
[25] Fundación Galileo Galilei—INAF, Rambla José Ana Fernandez Pérez 7, E-38712 Breña Baja, Tenerife, Spain

Abstract

The extreme environments of ultra-short-period planets (USPs) make excellent laboratories to study how exoplanets obtain, lose, retain, and/or regain gaseous atmospheres. We present the confirmation and characterization of the USP TOI-1347 b, a $1.8 \pm 0.1\,R_\oplus$ planet on a 0.85 day orbit that was detected with photometry from the TESS mission. We measured radial velocities of the TOI-1347 system using Keck/HIRES and HARPS-N and found the USP to be unusually massive at $11.1 \pm 1.2\,M_\oplus$. The measured mass and radius of TOI-1347 b imply an Earth-like bulk composition. A thin H/He envelope ($>0.01\%$ by mass) can be ruled out at high confidence. The system is between 1 and 1.8 Gyr old; therefore, intensive photoevaporation should have concluded. We detected a tentative phase-curve variation (3σ) and a secondary eclipse (2σ) in TESS photometry, which, if confirmed, could indicate the presence of a high-mean-molecular-weight atmosphere. We recommend additional optical and infrared observations to confirm the presence of an atmosphere and investigate its composition.

---

[26] NSF Graduate Research Fellow.
[27] NASA Sagan Fellow.
[28] NASA FINESST Fellow.
[29] NSF Astronomy and Astrophysics Postdoctoral Fellow.
[30] Henry Norris Russell Fellow.

1. Introduction

Ultra-short-period planets, or USPs, are exoplanets that orbit their stars with short orbital period (<1 day). USPs tend to not exceed $2\,R_\oplus$ in size, save for the closest of the hot Jupiter (HJ) population. This "hot-Neptune desert" (Mazeh et al. 2016) has been hypothesized to be sculpted by mass-loss mechanisms, such as photoevaporation (Owen & Wu 2017) or core-powered mass loss (Gupta & Schlichting 2019). Such mechanisms destroy the atmospheres of smaller planets, whereas giant

planets can better resist mass loss (in fact, HJ atmospheres can become inflated; Batygin et al. 2011; Grunblatt et al. 2017). The Kepler mission (Borucki et al. 2010) took the first steps to map out the demographics of close-in transiting planets and revealed that USPs exist around ~0.5%–0.8% of GK stars (Sanchis-Ojeda et al. 2014). Another key discovery from Kepler was the "radius gap" around 1.7–$1.9\,R_\oplus$, which separated the bimodal peaks corresponding to the smaller super-Earth population (no atmosphere) and the larger sub-Neptunes ($\gtrsim 1\%$ H/He atmosphere; Fulton et al. 2017; Fulton & Petigura 2018).

To date, only two nongiant USPs have been discovered with radii larger than $2\,R_\oplus$. TESS Object of Interest (TOI) 849 b (Armstrong et al. 2020) is a massive (~$40\,M_\oplus$), rocky world that is likely the stripped core of a giant planet (perhaps via giant collisions). LTT-9779 b ($29\,M_\oplus$, 0.79 day; Jenkins et al. 2020) defies its environment with a substantial (9% by mass) H/He atmosphere and a $4.6\,R_\oplus$ radius. This suggests some USPs can retain atmospheres. If so, where is the boundary between bare rocky cores and those with residual (or secondary) atmospheres?

A close-in orbiting planet will reflect starlight and emit thermal radiation, causing the observed brightness of the system to vary with the planet's orbital position. This variation, called the phase curve, depends on the planet's albedo and day–night temperature contrast. Phase-curve variations have been used to directly probe the surfaces of several USPs, finding some to be bare rock (LHS 3844b; Kreidberg et al. 2019; Kane et al. 2020) and others to perhaps possess high-mean-molecular-weight atmospheres (55 Cnc e; Demory et al. 2016).

Unlike Kepler, which observed a single patch of sky for 4 yr, the Transiting Exoplanet Survey Satellite (TESS; Ricker et al. 2015) is an all-sky transit survey that has discovered thousands of close-in planets around nearby bright stars that are amenable to radial velocity (RV) follow-up measurements. RVs provide key insight into the existence of exoplanetary atmospheres by measuring the planet's mass, thereby constraining the bulk density, planet surface gravity (which is related to atmospheric scale height), and its ability to resist photoevaporation. Our collaboration, the TESS-Keck Survey (TKS; Chontos et al. 2022), has been monitoring 86 TESS systems with RV follow-up using the HIgh Resolution Echelle Spectrometer (HIRES; Vogt et al. 1994) at the Keck I Telescope. As part of TKS, we have measured the masses of several USPs, such as TOI-561 b (Weiss et al. 2021) and TOI-1444 b (Dai et al. 2021), both of which have rocky compositions. In this paper, we present the discovery and mass measurement of the USP TOI-1347 b. The heaviest of the nongiant USPs[31] to date, TOI-1347 b shows hints of phase-curve variability and a secondary eclipse in its TESS photometry, which may indicate the presence of a high-mean-molecular-weight atmosphere. We also detected a second transiting planet in the system at 4.84 d, TOI-1347 c, in line with the common trend for USPs to have nearby outer companions that can shepherd the migrations of their USPs into their present sub-day orbits (Millholland & Spalding 2020).

This paper is structured as follows. In Section 2 we characterize the host star using spectroscopy. We rule out stellar companions using speckle imaging in Section 3. In Section 4 we analyze the TESS light curve to measure the

stellar rotation period, planetary transits, and tentative phase-curve variability and secondary eclipse. In Section 5 we present our RV measurements and the resulting mass constraints for both planets. Finally, we discuss the implications of our observations for the TOI-1347 system in Section 6.

2. Host Star Properties

2.1. Spectroscopic Properties

TOI-1347 (TIC 229747848) is a late G-type ($T_{\rm eff} = 5464 \pm 100$ K) star that is relatively active ($\log R'_{\rm HK} = -4.66$), showing strong variability in both photometry (see Section 4) and RVs (see Section 5).

We obtained high-resolution spectra of TOI-1347 with HIRES (with the B3 decker, $R = 67{,}000$) and the High Accuracy Radial Velocity Planet Searcher-North (HARPS-N; $R = 115{,}000$); see Section 5 for details. We applied the SpecMatch-Synthetic (Petigura 2015) algorithm to the HIRES spectrum to measure $T_{\rm eff}$, $M_\star$, Fe/H, and $\log g$. These parameters, as well as the J and K magnitudes from the TICv8 catalog (Paegert et al. 2021) and the Gaia parallax (Gaia Collaboration et al. 2023), were input into *isoclassify* (Huber et al. 2017; Berger et al. 2020) to constrain $R_\star$. We also used KeckSpec (A. Polanski 2024, in preparation) to compute alpha elemental abundances. Stellar parameters for TOI-1347 are included in the catalog of MacDougall et al. (2023). We verified that our values agree with the values therein to within 1σ.

We similarly derived spectroscopic parameters from the coadded HARPS-N spectra of TOI-1347 using the FASMA spectral synthesis package (Tsantaki et al. 2018, 2020). We verified that all derived quantities were in agreement with the HIRES values. In particular, the HARPS-N data are of sufficient resolution to detect $v \sin i_\star$, whereas with HIRES we only obtain an upper limit. Table 1 lists our adopted stellar parameters.

2.2. Age

We constrained the age of the host star using several methods. Using a stellar rotation period of 16.1 ± 0.3 days (see Section 4.1 for details), we estimated the gyrochronological age of the star. The scaling relation of Mamajek & Hillenbrand (2008) gives an age of 1.33 ± 0.06 Gyr. Using the latest empirical relations of Bouma et al. (2023), the age is 1.7 ± 0.1 Gyr. We also obtained an age estimate using chromospheric activity in the Ca II H and K lines from our HIRES spectra. We measured $\log R'_{\rm HK} = -4.66 \pm 0.05$ using the method of Isaacson & Fischer (2010). Combining with the calibration of Mamajek & Hillenbrand (2008), the corresponding age is 1.6 ± 0.4 Gyr. We also looked for the lithium doublet in our HIRES spectra but were unable to detect the lithium doublet above the noise floor in the continuum (see Figure 1). We placed an upper limit of 2 m Å (95% confidence) on the equivalent width. According to Berger et al. (2018), the star is consistent with field stars and is most likely older than the Hyades cluster (~650 Myr). Lastly, MacDougall et al. (2023) derived an age of $0.8^{+1.1}_{-0.6}$ Gyr from isochronal fitting.

The age uncertainties above do not account for systematic errors. Therefore, we combined age indicators with an unweighted mean. We adopted a wide age uncertainty of 0.4 Gyr to reflect the systematic uncertainties between the different age estimators. Our best age estimate for TOI-1347 is

---

[31] Other than the exceptional LTT-9779 b and TOI-849 b, which likely belong to a separate class of planets than the $\lesssim 10\,M_\oplus$ USPs (Dai et al. 2021).

Table 1
Stellar Parameters of TOI-1347

Parameter	Value	Unit	Source
TIC ID	TIC 229747848	⋯	TIC v8.2[a]
R.A.	18:41:18.4	hh:mm:ss	TIC v8.2[a]
Decl.	+70:17:24.19	dd:mm:ss	TIC v8.2[a]
V magnitude	11.168 ± 0.013	⋯	TIC v8.2[a]
TESS magnitude	10.7157 ± 0.0066	⋯	TIC v8.2[a]
J magnitude	10.011 ± 0.02	⋯	TIC v8.2[a]
K magnitude	9.616 ± 0.015	⋯	TIC v8.2[a]
Gaia magnitude	11.2076 ± 0.0005	⋯	Gaia DR3[b]
Parallax	6.7803 ± 0.0112	mas	Gaia DR3[b]
R.A. proper motion	-6.0883 ± 0.0150	mas yr^{-1}	Gaia DR3[b]
Decl. proper motion	26.1020 ± 0.0150	mas yr^{-1}	Gaia DR3[b]
Galactic U	-5.31 ± 0.09	km s^{-1}	Derived from Gaia DR3 astrometry[c]
Galactic V	-7.72 ± 0.46	km s^{-1}	Derived from Gaia DR3 astrometry[c]
Galactic W	4.91 ± 0.23	km s^{-1}	Derived from Gaia DR3 astrometry[c]
Luminosity	0.55 ± 0.02	$L_\odot$	Isoclassify[d]
Radius	0.83 ± 0.03	$R_\odot$	Isoclassify[d]
Mass	0.913 ± 0.033	$M_\odot$	SpecMatch-Synthetic[e]
$T_{\rm eff}$	5464 ± 100	K	SpecMatch-Synthetic[e]
$\log g$	4.64 ± 0.10	⋯	SpecMatch-Synthetic[e]
[Fe/H]	0.04 ± 0.06	dex	SpecMatch-Synthetic[e]
$[\alpha/{\rm Fe}]$	-0.03 ± 0.06	dex	KeckSpec[f]
$v \sin i_\star$	<3	km s^{-1}	SpecMatch-Synthetic[e]
$v \sin i_\star$	2.9 ± 0.1	km s^{-1}	FASMA[g]
v_{eq}	2.61 ± 0.11	km s^{-1}	From $P_{\rm rot}$ and R_*
$\log R'_{\rm HK}$	-4.66 ± 0.05	⋯	From Keck/HIRES spectrum
$P_{\rm rot}$	16.1 ± 0.3	days	From ACF of TESS photometry (Section 4.1)
$P_{\rm rot}$	16.3 ± 0.6	days	From TESS-SIP with TESS photometry (Section 4.1)
$P_{\rm rot}$	16.2 ± 0.3	days	From GP fit to RVs (Section 5.1)
Age	1.7 ± 0.1	Gyr	From $P_{\rm rot}$ using empirical relations of Bouma et al. (2023)
Age	1.33 ± 0.06	Gyr	From $P_{\rm rot}$ using empirical relations of Mamajek & Hillenbrand (2008)
Age	1.6 ± 0.4	Gyr	From $\log R'_{\rm HK}$ using empirical relations of Mamajek & Hillenbrand (2008)
Age	$0.8^{+1.1}_{-0.6}$	Gyr	From isochronal fitting by MacDougall et al. (2023)
Age	>650	Myr	From Li and comparison to Hyades (Berger et al. 2018)
Age	1.4 ± 0.4	Gyr	Adopted value

Notes.
[a] Paegert et al. (2021).
[b] Gaia Collaboration et al. (2023).
[c] Using local standard of rest from Coşkunoğlu et al. (2011), as implemented in PyAstronomy.pyasl.gal_uvw (Czesla et al. 2019).
[d] Huber et al. (2017), using the SpecMatch-Synthetic results from an HIRES spectrum. Uncertainties are random errors for the adopted model grid. To account for systematic errors, see Tayar et al. (2022).
[e] Petigura (2015), using an HIRES spectrum taken at $R \sim 67{,}000$ with no iodine.
[f] A. Polanski (2024, in preparation), using a HIRES spectrum taken at $R \sim 67{,}000$ with no iodine.
[g] Tsantaki et al. (2018, 2020), using the coadded HARPS-N spectra.
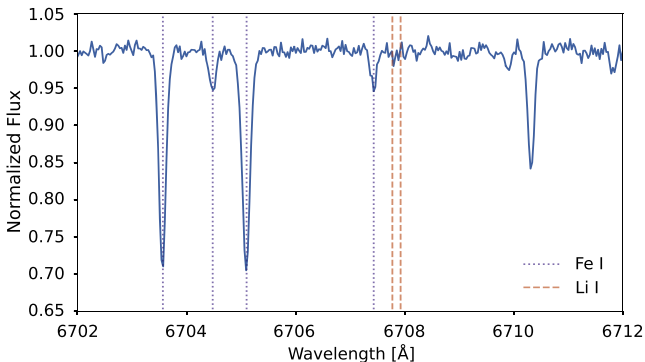
Figure 1. HIRES spectrum of TOI-1347 in the neighborhood of the lithium doublet. Nearby Fe I lines are labeled. No absorption attributed to lithium was detected.

thus 1.4 ± 0.4 Gyr. Importantly, this age is longer than the timescale on which photoevaporation operates, which is typically confined to the first few hundred megayears when the star is active in X-rays and extreme UV (Ribas et al. 2005; Tu et al. 2015).

3. High-resolution Imaging

To help validate the transiting planets, we observed TOI-1347 with the 'Alopeke (Scott et al. 2021) dual-channel speckle imaging instrument on Gemini-N (PI: Crossfield) with a pixel scale of $0\farcs01\,{\rm pixel}^{-1}$ and a full width at half maximum resolution of $0\farcs02$. With 'Alopeke we obtained simultaneous speckle imaging at 562 and 832 nm, with a total of seven observing blocks each consisting of one thousand 60 ms exposures.
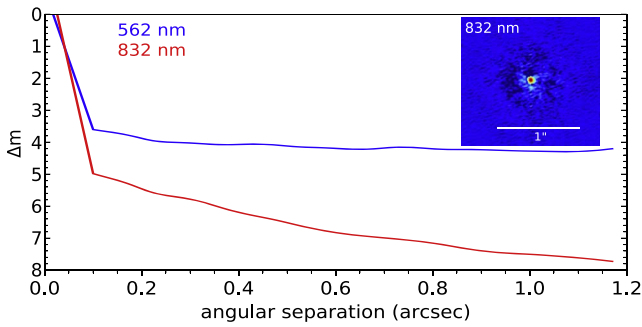
Figure 2. Contrast curves around TOI-1347 from Gemini/'Alopeke; the inset shows the reconstructed image at 832 nm. No companions are detected.

We processed these images with the speckle pipeline of Howell et al. (2011), which yielded the 5σ sensitivity curves and reconstructed image shown in Figure 2. The curves do not show companions at angular separations of $0''5$ or greater at a contrast of 4.12 mag at 562 nm and 6.52 mag at 832 nm (Figure 2).

4. TESS Photometry

TOI-1347 was observed by TESS in sectors 14–26, 40, 41, and 47–60, which span UT 2019 July 18 to 2023 January 18. The Science Processing Operations Center (SPOC; Jenkins et al. 2016) detected two transiting planet candidates that were subsequently diagnosed and vetted as TOIs 1347.01 (b) and 1347.02 (c) (Guerrero et al. 2021).

We downloaded the 20 and 120 s cadence SPOC light curves using lightkurve (Lightkurve Collaboration et al. 2018). We removed all data points with a nonzero quality flag, i.e., those suffering from cosmic rays or other known systematic issues. We then stitched and normalized the multisector data using lightkurve and applied a 5σ clipping. lightkurve also provides the correction for scattered light (2% contamination reported by ExoFOP). The resulting light curve, shown in Figure 3, exhibits significant but coherent periodic variability corresponding to rotationally modulated surface inhomogeneities on the stellar disk.

4.1. Stellar Rotation Period

The effect of a starspot on photometry is to reduce the observed (integrated) intensity when on the visible hemisphere. The net effect of many spots is quasiperiodic variability that can be treated as time-correlated noise (Haywood et al. 2014; Rajpaul et al. 2015; Aigrain & Foreman-Mackey 2023). The TESS photometry of TOI-1347 shows strong rotational variability with maxima/minima occurring roughly every ~8 days (see the top panel in Figure 3). A Lomb–Scargle periodogram of the photometry shows a strong peak at 8 days (Figure 4). However, a closer examination of the light curve reveals that the depths of adjacent maxima/minima are dissimilar. In fact, the depths of alternating maxima/minima tend to have similar amplitudes. This can be explained if the star has a 16 day rotation period and multiple spot groups concentrated on opposite hemispheres of the star, an effect noted for a number of other stars (Holcomb et al. 2022). In fact, a periodogram analysis of the RV data set shows a strong peak at 16 days (Figure 4). Spots affect RVs in much the same way as photometry by breaking the flux balance across star's

rotational velocity profile (Saar & Donahue 1997), in addition to suppressing the convective blueshift (Haywood et al. 2016).

While the periodogram is essentially a Fourier decomposition showing the amplitude of the best-fitting sine wave at all possible periods, the autocorrelation function (ACF) measures the self-similarity of a time series as a function of time delay. Thus, if the variability in a time series is not sinusoidal (asymmetric, more complex shape), then the ACF will give a better estimate of the periodicity than the periodogram. The ACF of the TESS photometry has its highest peak at ~16 days (Figure 3) with adjacent ACF peaks alternating between high and low amplitude. An analysis of the ACF using spin-spotter (Holcomb et al. 2022) successfully identified the half-period effect by checking that the odd peaks are less than 10% the height of the even peaks. spinspotter returns a rotation period of $P_{\rm rot} = 16.1 \pm 0.3$ days by averaging the locations of the even-numbered peaks only. We also measured the stellar rotation period using the TESS Systematics Insensitive Periodogram (TESS-SIP) algorithm (Hedges et al. 2020). TESS-SIP simultaneously corrects for instrument systematics while performing the periodogram search on the TESS Simple Aperture Photometry. Using TESS-SIP for sectors 14–26 for TOI-1347, we measured a stellar rotation period of 16.34 ± 0.57 days.

With all of this considered, we adopt the ~16 day solution as the rotation period of TOI-1347 and explain the Lomb–Scargle periodogram peak at $P_{\rm rot}/2$ as arising from antipodal spot groups. The persistence of repeated peaks every 8 days in the ACF, even out to beyond 100 days, can be explained if the starspots on TOI-1347 live for many rotation periods. Following the prescription of Giles et al. (2017), we fit the observed ACF with an underdamped simple harmonic oscillator, including a second component with power at $P/2$:

$$y = e^{-\Delta t/\tau}\left[A\cos\left(\frac{2\pi\Delta t}{P}\right) + B\cos\left(\frac{2\pi\Delta t}{P/2}\right) + y_0,\right]. \quad (1)$$

In Equation (1), y is the ACF strength, and the coefficients A and B give the relative strengths of the antipodal spot groups. We used scipy.optimize (Virtanen et al. 2020) to find the maximum a posteriori (MAP) solution, then used that as a seed for a Markov Chain Monte Carlo (MCMC) analysis using emcee (Foreman-Mackey et al. 2013). The fit recovered $P = 16.0$ days, and the best-fit exponential decay timescale was $\tau = 45$ days, roughly 3 times the rotation period. Both coefficients $A = 0.05$ and $B = 0.18$ were constrained to nonzero values, again supporting the multiple spot group hypothesis.

Lastly, our SpecMatch-Synthetic analysis of the HIRES spectrum in Section 2.1 yielded only an upper limit corresponding to the line spread function of HIRES (roughly 2.2 km s^{-1}). Masuda et al. (2022) recently showed that on the population level, such nondetections of $v\sin i_\star$ are most consistent with a <3 km s^{-1} upper limit. Combining $P_{\rm rot} = 16.1$ days with the stellar radius from Section 2.1, we get an equatorial rotational velocity of $v_{\rm eq} = 2.6 \pm 0.1$ km s^{-1}. This is consistent with a <3 km s^{-1} upper bound for HIRES though it is slightly smaller than the measured HARPS-N value. Were the rotation period 8 days, we would instead have $v_{\rm eq} \sim 5$ km s^{-1}, which (barring a misaligned stellar inclination of $\lesssim 30°$) would be detectable in the HIRES spectrum and inconsistent with the HARPS-N measurement. If astrophysical, the slightly larger
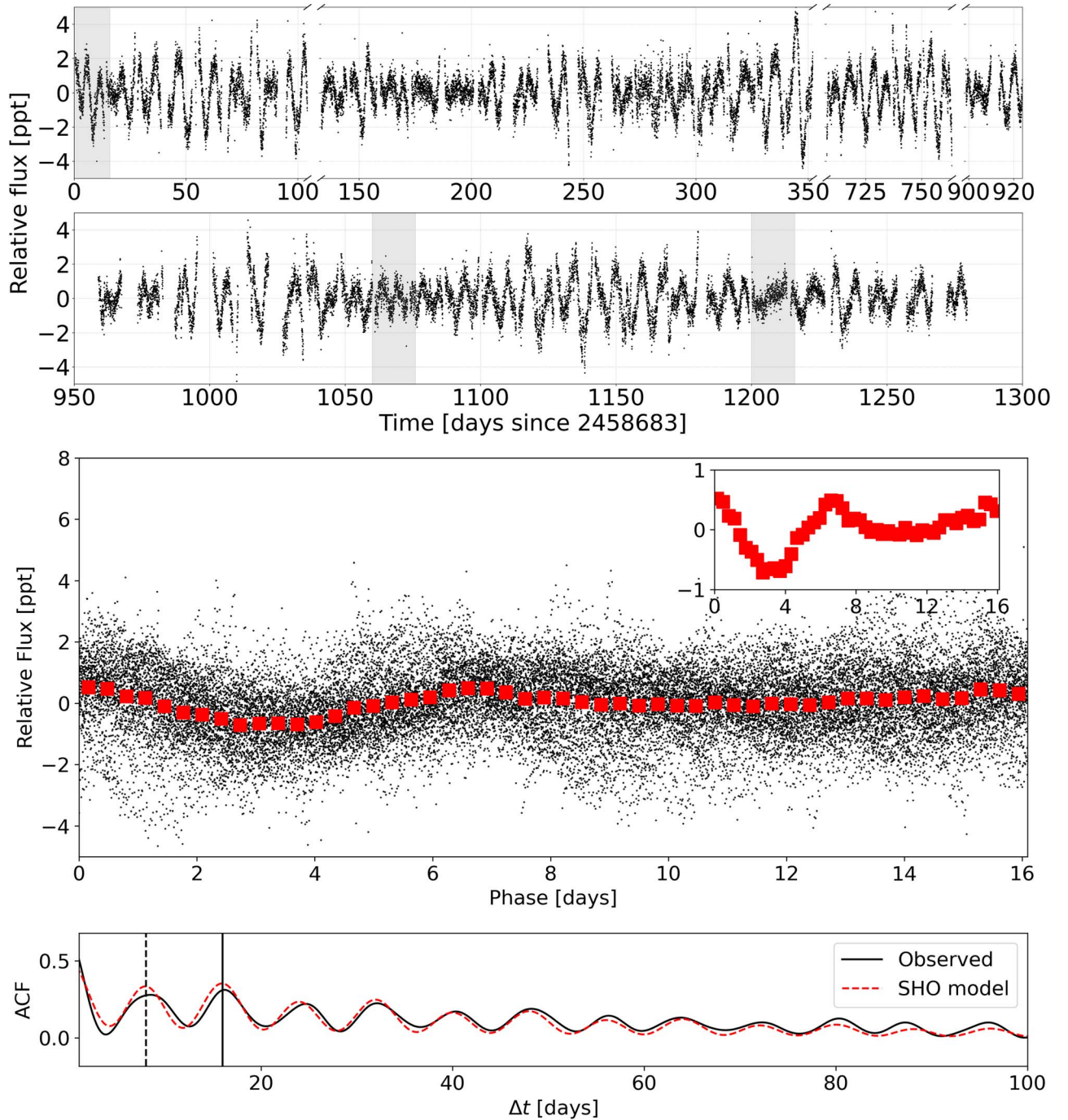
Figure 3. Top: the full 120 s cadence SPOC TESS light curve, binned to 30 minutes. Rotationally modulated variability is strong and evolves over time; the three shaded regions highlight example 16 day windows in which different numbers of maxima/minima are observed. Middle: the 30 minute light curve phased to the 16.1 day rotation period. The red points further bin the folded data to ∼8 hr bins. The inset zooms in on these binned phased data and highlights the tendency for every other set of maximum/minimum to repeat in amplitude. Bottom: the ACF of the photometry, showing regular peaks at all multiples of 8 days (dashed line) with the highest peak at 16 days (dark line). The red dashed line shows the best-fit SHO model described in Section 4.1.

$v \sin i_\star$ could be explained by differential rotation and long-lived starspots at higher latitudes.

4.2. Additional Transiting Planets?

We searched the TESS light curve for planetary transits with a Box-fitting Least Squares (BLS; Kovács et al. 2002) algorithm as described in Dai et al. (2021). We recovered the two planet candidates reported by ExoFOP at 0.84 and

4.84 days. We did not find any other transit signals with signal-to-noise ratio (S/N) > 6.5.

4.3. Transit Modeling

Our transit analysis closely follows that described in Dai et al. (2021). Briefly, we generated transit signals using the Python package Batman (Kreidberg 2015), parameterized with the stellar density ($\rho_\star$) to break the degeneracy between the scaled semimajor axes ($a/R_\star$) and impact parameters (b) of
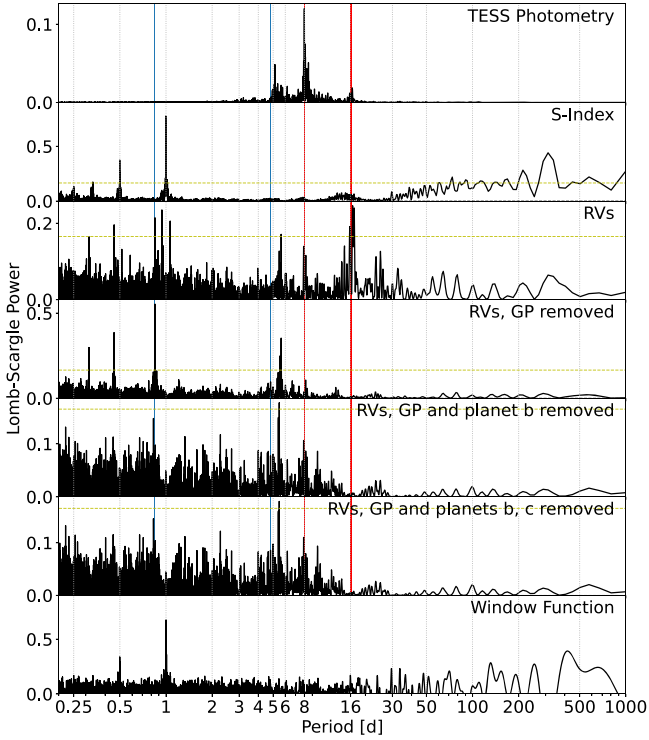
Figure 4. Lomb–Scargle periodograms of, from top to bottom, the TESS photometry, S-Indices, RVs and RVs with the GP model (Section 5.1) removed, the GP-corrected RVs with the Keplerian model for the USP subtracted, the GP-corrected RVs with both planets subtracted, and the window function (Dawson & Fabrycky 2010) of the RV time series. The periodograms are computed using `astropy.timeseries.LombScargle` (Astropy Collaboration et al. 2022). The blue lines correspond to the orbital periods of TOI-1347 b and c, and the two dark red lines are drawn at 8 days (thin) and 16 days (thick). The horizontal yellow line is the 1% false alarm probability.

the transiting planets (Seager & Mallén-Ornelas 2003). We imposed a prior using the best-fit stellar density from our adopted M_* and R_* of $\rho_* = 2.25 \pm 0.26$ g cm^{-3}. For the limb darkening coefficients, we used the prior and parameterization scheme of Kipping (2013) for a quadratic limb darkening law (q_1 and q_2). The other transit parameters included the orbital period (P_{orb}), time of conjunction (T_c), planet-to-star radius ratios (R_p/R_*), scaled orbital distances (a/R_*, computed from stellar density and orbital period), orbital inclinations (cos$i$), orbital eccentricities (e), and the arguments of pericenter (ω). We initially allowed nonzero eccentricities for both TOI-1347 b and c; however, the posterior distributions are fully consistent with circular orbits. Neither the existing transit nor RV data (Section 5) support the detection of nonzero eccentricities. In our final fits, we chose to restrict both planets to circular orbits to reduce model complexity.

Our transit fitting pipeline takes the following steps:

1. Fit a global model of all transit epochs, assuming no transit timing variations (TTVs). This model is found by maximizing the likelihood with the Levenberg–Marquardt method implemented in Python package `lmfit` (Newville et al. 2014).

2. Search for TTVs. We held the transit shape parameters fixed and fit for the mid-transit times of each transit epoch. We removed out-of-transit variations with a quadratic model. We did not detect significant TTVs for either planet, so we continued with fixed orbital periods.
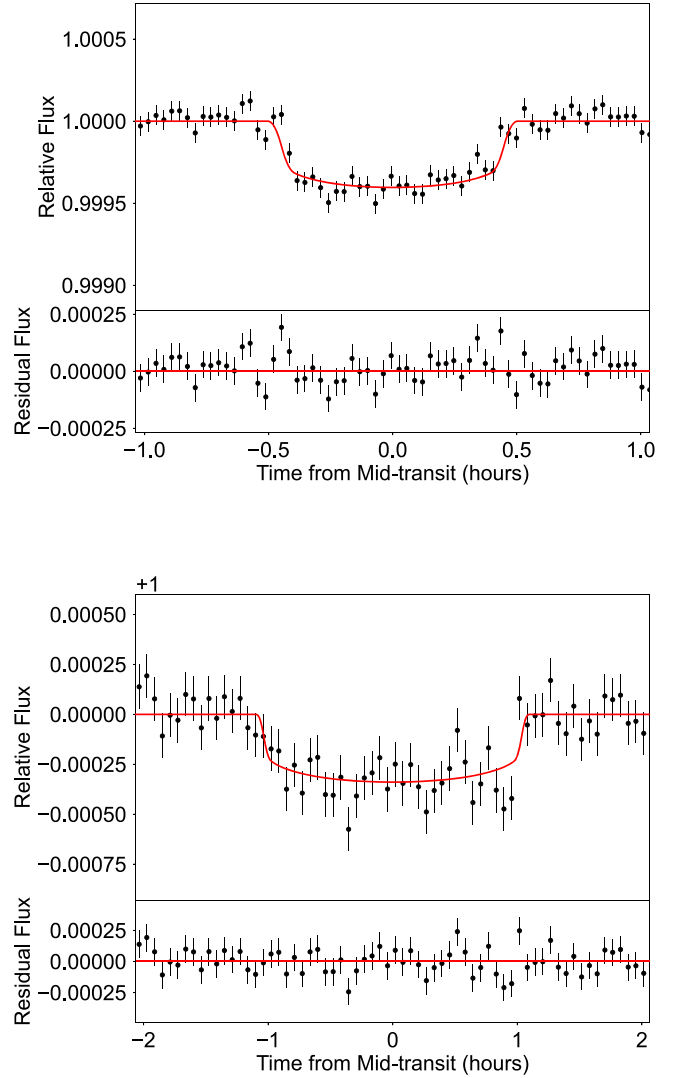
Figure 5. The 2 minute TESS light curves phase folded and binned using the orbital periods of TOI-1347 b (top) and c (bottom). The best-fit transit models are shown with red solid lines.

3. Full model. We sampled the posterior distributions of both planets jointly using the MCMC framework implemented in *emcee* (Foreman-Mackey et al. 2013) with 128 walkers initialized near the MAP solution. We ran `emcee` for 50,000 steps, ensuring that this was many times longer than the autocorrelation of various parameters (typically 100 s of steps).

Figure 5 shows the phase-folded and binned transits of TOI-1347 b and c with the MAP model. Using the stellar radius derived in Section 2, we derived $R_{p,b} = 1.8 \pm 0.1\, R_\oplus$ and $R_{p,c} = 1.6 \pm 0.1\, R_\oplus$, in agreement with the radii measured by MacDougall et al. (2023; $R_{p,b} = 1.81^{+0.09}_{-0.06}\, R_\oplus$ and $R_{p,c} = 1.68^{+0.09}_{-0.07}$).

4.4. Phase Curve

We searched the TESS light curve for phase-curve variations and secondary eclipses of TOI-1347 b. First, we masked the in-transit data and removed long-term variability (stellar and/or instrumental) using the method of Sanchis-Ojeda et al. (2013). This involves fitting a linear function of time to the out-of-
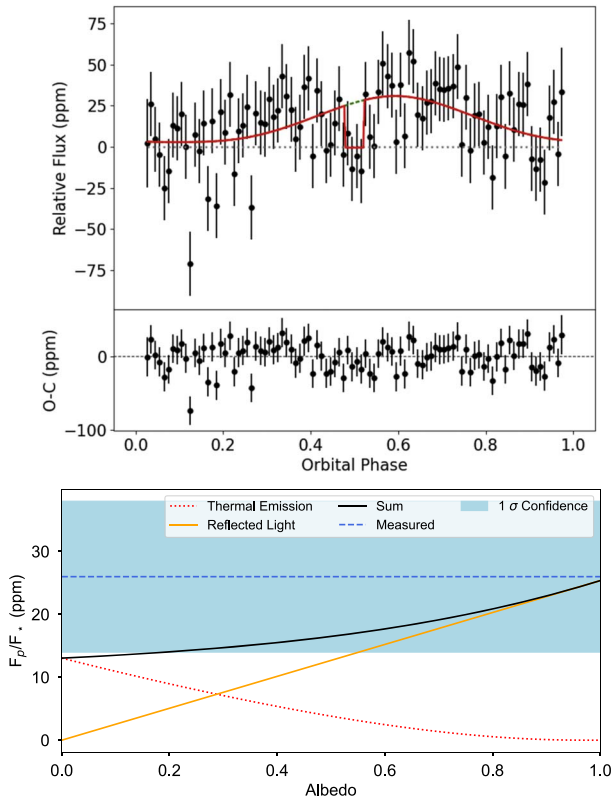
Figure 6. Upper: the phase curve and secondary eclipse of TOI-1347 b as observed by TESS. The best-fit model is shown by the red curve. The green dotted line gives the model with no eclipse. The phase curve is detected at the 2σ level. It is likely a combination of thermal emission and reflected light in the TESS band (600–1000 nm). Lower: the thermal emission (red dotted line) and reflected light (orange solid line) from TOI-1347 b as a function of the Bond albedo. The blue dashed line and shaded area are the measured secondary eclipse depth (F_p/F_*) and its 1σ central interval.

transit data points within a window of $2\times$ the orbital period, then dividing the best-fit function within that window, repeating for every data point in the light curve. This detrended light curve is then phase folded to the orbital period of TOI-1347 b.

The resultant phase curve is shown in Figure 6. We were able to detect a tentative phase-curve variation (3σ) and a secondary eclipse (2σ) using a joint model. To model the secondary eclipse, we simply modified the best-fit transit model by shifting the mid-transit times by half the orbital period (i.e., assuming $e = 0$) and turning off limb darkening ($q_1 = q_2 = 0$). The secondary eclipse depth ($\delta_{\rm sec}$) is allowed to vary freely to account for a combined effect of reflected stellar light and thermal emission from the planet's nightside. For the phase curve, we used a Lambertian disk model (see, e.g., Demory et al. 2016) parameterized by an amplitude A and phase offset of the peak θ. We sampled the posterior distribution with an MCMC analysis similar to that described in Section 4.3. We found a secondary eclipse depth of $\delta_{\rm sec} = 26 \pm 12$ ppm and a phase-curve amplitude of $A = 28 \pm 9$ ppm. The peak of the phase-curve variation is shifted by $33° \pm 14°$ to the west of the planet.

The lower panel of Figure 6 compares the amount of thermal emission versus reflected light as a function of the planet's Bond albedo (A_B). At high albedo, the planet is more reflective, and the equilibrium temperature will be lower. In this case, the phase curve will be dominated by reflected stellar light rather than thermal emission. This is necessary to explain the large secondary eclipse depth measured in the TESS band. Moreover, we marginally detected a phase offset of $33° \pm 14°$ to the west of the planet. Both of these effects can be explained if TOI-1347 b is retaining a high-mean-molecular-weight atmosphere. Silicate clouds in this atmosphere could produce a high albedo, while partial cloud coverage may produce the observed phase offset to the West (see, e.g., Kepler-7 b, Demory et al. 2013). However, the data in hand are insufficient to definitively confirm the presence of an atmosphere on TOI-1347 b. Higher S/N follow-up observations with JWST are required.

5. Radial Velocities

We collected 120 high-resolution optical spectra of TOI-1347 between UT 2019 November 28 and UT 2022 July 26 with HIRES on the Keck I telescope as part of TKS (Chontos et al. 2022). We took exposures using the "C2" decker ($R = 45,000$) and integrated until the exposure meter reached 60,000 counts (S/N $\sim$100 per reduced pixel), which resulted in a typical exposure time of 648 s. We used the standard procedures of the California Planet Search (Howard et al. 2010) to reduce the HIRES spectra and extract precise RVs using the iodine cell for wavelength calibration (Butler et al. 1996). The average Doppler precision per measurement was $1.83\,\mathrm{m\,s^{-1}}$.

We also obtained 14 spectra with the HARPS-N , installed at the Telescopio Nazionale Galileo (Cosentino et al. 2012). Observations were taken with 1800 s exposure times (average S/N is 42.3 in order 50) with simultaneous wavelength calibration provided by the Fabry–Perot etalon. Cross-correlation functions (CCFs) were created using the ESPRESSO G2 mask, and RVs were extracted by fitting for the CCF centroid (Dumusque et al. 2021). Before jointly fitting with the HIRES RVs, we subtracted the median RV from the HARPS-N data set.

See Table 3 for the full RV data set, which includes Mount Wilson S-Index values derived from the Ca II H and K lines (Duncan et al. 1991) for the HIRES data. The $S_{\rm HK}$ index shows a weaker power excess around $P_{\rm rot}$ in a Lomb–Scargle periodogram than the RVs (Figure 4) but are primarily dominated by a 1 day sampling alias. The $S_{\rm HK}$ indices are correlated with the RVs at the 3.5σ level with a Pearson correlation coefficient of 0.31 (p-value of 0.0005). This weak correlation is likely why our models in Section 5.1 that were trained on the S-Index time series did not improve the overall fit.

5.1. RV Model

We chose to adopt the same two-component simple harmonic oscillator (SHO) model for our RV model that we used to model stellar variability in photometry. We used the `exoplanet` (Foreman-Mackey et al. 2021) package to construct a Gaussian process (GP) stellar activity model with a kernel defined by the built-in `RotationTerm` parameterization. This kernel is a mixture of two SHOs analogous to the first and second cosine terms in Equation (1). We also tried a GP with the quasiperiodic kernel implemented in `radvel` (Fulton et al. 2018), both untrained and trained on the S-Indices. We found that the quasiperiodic kernel struggled to identify a single primary period, often jumping between 8 and 16 days. In order for the MCMC to converge, a reasonably

Table 2
Transit and RV Parameters of the TOI-1347 System

Parameter	Symbol	Prior	Posterior Distribution	Unit
TOI-1347 b				
Planet/Star Radius Ratio	$R_p/R_\star$	Uniform(-10, 10) on $\ln(R_p/R_\star)$	0.02039 ± 0.00072	...
Time of Conjunction	T_c	Uniform(1682, 1683)	1682.71214 ± 0.00060	(BJD-2457000)
Orbital Period	$P_{\rm orb}$	Uniform(-10, 10) on $\ln(P_{\rm orb})$	$0.84742346 \pm 0.00000061$	days
Orbital Inclination	$i_{\rm orb}$	Uniform(-1, 1) on $\cos i_{\rm orb}$	79.5 ± 0.7	deg
Orbital Eccentricity	e	...	0 (fixed)	...
Impact Parameter	b	Derived	0.82 ± 0.03	...
Scaled Semimajor Axis	$a/R_\star$	Derived	4.43 ± 0.21	...
RV Semiamplitude	K	Normal(0, 50)	$7.74^{+0.80}_{-0.79}$	m s^{-1}
Planetary Radius	$R_{\rm p}$	Derived	1.8 ± 0.1	$R_\oplus$
Planetary Mass	$M_{\rm p}$	Derived	11.1 ± 1.2	$M_\oplus$
Bulk Density	ρ	Derived	$9.9^{+2.1}_{-1.7}$	g cm^{-3}
Equilibrium Temperature	$T_{\rm eq}$	Derived ($A_B = 0.7$)	1400 ± 40	K
TOI-1347 c				
Planet/Star Radius Ratio	$R_p/R_\star$	Uniform(-10, 10) on $\ln(R_p/R_\star)$	0.0179 ± 0.0010	...
Time of Conjunction	T_c	Uniform(1678, 1679)	1678.5059 ± 0.0021	(BJD-2457000)
Orbital Period	$P_{\rm orb}$	Uniform(-10, 10) on $\ln(P_{\rm orb})$	4.841962 ± 0.000012	days
Orbital Inclination	i	Uniform(-1, 1) on $\cos i_{\rm orb}$	87.5 ± 0.4	deg
Orbital Eccentricity	e	...	0 (fixed)	...
Impact Parameter	b	Derived	0.73 ± 0.08	...
Scaled Semimajor Axis	$a/R_\star$	Derived	14.18 ± 0.49	...
RV Semiamplitude	K	Normal(0, 50)	$1.08^{+0.91}_{-0.92}$ (<2.59 at 95%)	m s^{-1}
Planetary Radius	$R_{\rm p}$	Derived	1.6 ± 0.1	$R_\oplus$
Planetary Mass	$M_{\rm p}$	Derived	2.8 ± 2.3 (< 6.4 at 95%)	$M_\oplus$
Bulk Density	ρ	Derived	$3.6^{+3.3}_{-3.0}$ (<4.1 at 95%)	g cm^{-3}
Equilibrium Temperature	$T_{\rm eq}$	Derived ($A_B = 0.1$)	1000 ± 25	K
Stellar Parameters				
Stellar Density	$\rho_\star$	Normal(2.25, 0.26)	2.30 ± 0.24	g cm^{-3}
Limb Darkening	q_1	Uniform(0, 1)	0.28 ± 0.20	...
Limb Darkening	q_2	Uniform(0, 1)	0.35 ± 0.28	...
HIRES RV Jitter	$\sigma_{\rm HIRES}$	HalfNormal(0, 10)	$4.05^{+0.73}_{-0.67}$	m s^{-1}
HARPS-N RV Jitter	$\sigma_{\rm HARPS}$	HalfNormal(0, 10)	$8.20^{+2.67}_{-1.98}$	m s^{-1}
GP Amplitude	$A_{\rm GP}$	InverseGamma(1, 5)	$9.70^{+1.16}_{-1.06}$	m s^{-1}
Rotation Period	$P_{\rm GP}$	Normal(ln(16), 0.5) on $\ln(P_{\rm GP})$	$16.16^{+0.35}_{-0.35}$	days
Oscillator Quality Factor	Q_0	HalfNormal(0, 2) on $\ln(Q_0)$	$1.49^{+0.74}_{-0.91}$	...
Quality Factor Difference	ΔQ	Normal(0, 2) on $\ln(\Delta Q)$	$1.71^{+1.32}_{-2.33}$	...
Fractional Amplitude	f	Uniform(0.1, 1)	$0.73^{+0.19}_{-0.24}$	...
Instrumental RV Parameters				
RV Offset (HIRES)	$\gamma_{\rm HIRES}$	Normal(0, 200)	$-2.12^{+0.90}_{-0.87}$	m s^{-1}
RV Offset (HARPS-N)	$\gamma_{\rm HARPS}$	Normal(0, 200)	$6.29^{+3.35}_{-3.41}$	m s^{-1}

strong prior (± 0.5 day or less) had to be placed on one of these period solutions. We found this undesirable compared to the SHO kernel in `exoplanet`, which was able to lock onto the 16 day period even with wide priors of >10 days. We also found the final fit to be statistically indistinguishable whether the GP was trained on the S-Indices or not, so for our final model we opted for an untrained SHO GP.

For the full mathematical definition of the SHO GP kernel, the interested reader is directed to Foreman-Mackey et al. (2017). In brief, the kernel is parameterized by the GP amplitude ($A_{\rm GP}$), the primary period of variability ($P_{\rm GP}$), the quality factor of the primary mode Q_0, the difference in quality factors between the period and half-period modes (ΔQ_0), and lastly the fractional amplitude between the two modes (f). We followed the guidance of the `exoplanet` tutorials to choose the appropriate priors on these parameters, which are tabulated in Table 2.

In practice, the Keplerian models are only parameterized by the RV semiamplitude K, which we place a wide, uninformative Gaussian prior on. We do not restrict K to positive values only, as such a prior can bias mass estimates to higher values, especially in the case of nondetections (Weiss & Marcy 2014). We imposed Gaussian priors on the periods and times of conjunction using the best-fit mean and standard deviation derived from our transit fits (Table 2), effectively fixing them to the tight transit constraints. Like the transit model, we fixed the eccentricity (e) and argument of periastron (ω) to zero. We included separate jitter terms for HIRES ($\sigma_{\rm HIRES}$) and HARPS-N ($\sigma_{\rm HARPS}$) and likewise separate RV offsets ($\gamma_{\rm HIRES}$) and HARPS-N ($\gamma_{\rm HARPS}$).

We initialized our model at the best-fit values from photometry, where applicable, and determined initial guesses for the RV semiamplitudes using `exoplanet.estimate_-semi_amplitude`. We then solved for the MAP solution

using `scipy.optimize.minimize`. The MAP parameters were then used as a seed for an MCMC exploration of the posterior. We employed a Hamiltonian Monte Carlo (HMC; Duane et al. 1987; Neal 2011) implemented in `PyMC3` (Salvatier et al. 2016), specifically the No-U-Turn Sampler (NUTS; Hoffman & Gelman 2014). HMC and NUTS are generally more efficient than the traditional Metropolis–Hastings algorithm (Metropolis et al. 1953; Hastings 1970), resulting in well-mixed MCMC chains in far fewer samples. We sampled with NUTS in four parallel chains for 5000 "tuning" steps, which are discarded. The number of tuning steps was chosen to obtain an acceptance fraction near the target of 0.9, which balances the number of retained samples and efficient exploration of the posterior space. Each chain then collects 5000 samples for a total of 20,000 posterior samples. We ensured adequate statistical independence among these samples by requiring that the per-parameter $\hat{R}$ statistic (Vehtari et al. 2021) be <1.001.

Our best-fitting RV model is shown in Figure 7. The GP robustly recovers a primary period of 16.2 ± 0.3 days, even with a wide prior, independently verifying our assessment of the stellar rotation period from photometry. The USP TOI-1347 b is also robustly detected at consistent semiamplitudes, regardless of the activity model used (trained/untrained, quasiperiodic/SHO). The resulting mass of TOI-1347 b is $11.1 \pm 1.2 \, M_\oplus$. The second planet, TOI-1347 c, is not detected in the RVs. We adopt an upper limit of $<6.4 \, M_\oplus$ at 95% confidence. The residual rms to the combined Keplerian + GP model is $4.9 \, \mathrm{m \, s^{-1}}$ for HIRES and $7.5 \, \mathrm{m \, s^{-1}}$ for HARPS-N, which is (expectedly) similar to the fitted stellar jitter values ($4.0 \pm 0.7 \, \mathrm{m \, s^{-1}}$ and $8.2^{+2.7}_{-2.0} \, \mathrm{m \, s^{-1}}$ respectively), but larger than the per-measurement uncertainty of each instrument (2.5 and $1.9 \, \mathrm{m \, s^{-1}}$).

Of note is the large jitter for the HARPS-N RVs. We suspect this is due to the GP being primarily conditioned on the HIRES RVs, resulting in poor predictive accuracy for activity during the timespan of the HARPS-N data, which occur about 1–2 rotation cycles before the HIRES data. As a result, the jitter term for HARPS-N is inflated to compensate. We tried to separate GPs for both data sets, sharing all hyperparameters except for the GP amplitude (A_{GP}). We found a nearly identical result (in fact, the best-fit HARPS-N jitter was higher) with statistically indistinguishable planet parameters, likely due to the relatively few HARPS-N data points. As a result, we adopt the single GP model but encourage further investigation into the nature of stellar activity on TOI-1347. As it stands, there are too few HARPS-N data points to condition independent GPs, but the single GP model is potentially overfitted to the HIRES points, reducing its out-of-sample predictive accuracy (Blunt et al. 2023).

6. Discussion

6.1. A Heavy Core Pushing the Limit of Photoevaporation

TOI-1347 b is the largest (in both mass and radius) of the super-Earth USPs to date. It seems to be rocky in composition and similar in iron core mass fraction to the Earth. Figure 8 shows the two planets in the context of known exoplanets on the mass–radius diagram.[32] We modeled the core composition of TOI-1347 b assuming a simple two-layer model with an iron

---

core and a silicate ("rock") mantle (Zeng et al. 2016). Our mass and radius measurements suggest an iron core mass fraction of $41\% \pm 27\%$, not far from Earth's 33% core mass fraction. TOI-1347 b joins a group of well-characterized USPs (Dai et al. 2019) that are consistent with an Earth-like composition.

With a core mass larger than $10 \, M_\oplus$, TOI-1347 b, along with the USPs TOI-1075 b (Essack et al. 2023) and HD 20329 b (Murgas et al. 2022), are close to the theoretical limit for runaway accretion (see, e.g., Rafikov 2006). How did these planets evade runaway accretion and not become gas giants? Lee (2019) and Chachan et al. (2021) both noted that the local hydrodynamic conditions, the envelope opacity, and the timescale of core assembly relative to disk dissipation could all contribute to quenching runaway accretion. As more of these systems are discovered, population-level analyses may shed light on which planets are able to evade runaway and which grow into gas giants.

TOI-1347 b also pushes the efficacy of photoevaporation to its limit. At $>10 \, M_\oplus$, the outflowing atmosphere has to overcome a deep gravitational potential well. On the other hand, the temperature of atmospheric outflows is likely capped below $10^4 \, \mathrm{K}$ due to strong radiative cooling at higher temperatures (see, e.g., Murray-Clay et al. 2009). An order-of-magnitude comparison reveals that the thermal sound speed ($\sim 10 \, \mathrm{km \, s^{-1}}$ at $10^4 \, \mathrm{K}$) may not overcome the escape velocity of the planet ($\sim 25 \, \mathrm{km \, s^{-1}}$ at $10 \, M_\oplus$ and $1.9 \, R_\oplus$), preventing bulk hydrodynamic outflow (i.e., photoevaporation). Previous models showed that photoevaporation is significantly quenched on planets with heavier cores ($\gtrsim 6 \, M_\oplus$; see, e.g., Owen & Wu 2017; Wang & Dai 2018). Planets like TOI-1347 b are therefore important test cases to understand the limit of both photoevaporation and core-powered mass loss (Ginzburg et al. 2018; Gupta & Schlichting 2019). Our mass and radius measurements disfavor the presence of a thick H/He envelope (Figure 8). Did TOI-1347 b have, and then lose, a primordial H/He envelope? Or, could TOI-1347 b have formed near to its present-day scorching orbit without ever acquiring a substantial atmosphere? We encourage further investigation on this question.

6.2. A Heavy-mean-molecular-weight Atmosphere?

Even though TOI-1347 b has a mass and radius that suggest an Earth-like bulk composition, we cannot rule out the presence of a heavy-mean-molecular-weight atmosphere. Lopez (2017) showed that the largest of the nongiant USPs (such as 55 Cnc e) can hold onto high-metallicity atmospheres even in the presence of strong stellar radiation. Such an atmosphere would only marginally inflate the planet's radius (the scale height of a CO_2-based atmosphere is about 11 km, while planetary radii are $\sim 10{,}000 \, \mathrm{km}$).

In fact, our tentative phase curve (3σ) and secondary eclipse (2σ) detections of TOI-1347 b point to a nonzero albedo and a possible phase offset to the west. These features could indicate the presence of an atmosphere at least partially covered by reflective silicate clouds. It may be the case that the deep gravitational wells of the most massive super-Earth USPs are sufficient to cling to such an atmosphere and resist atmospheric loss mechanisms. R. Hu et al. (2024, in preparation) show that their JWST NIRCam and MIRI observations of 55 Cnc e, a similar massive USP (0.73 day orbit; $9 M_\oplus$), can only be explained if the planet still has a CO- or CO_2-based atmosphere. Future observations with JWST might uncover a

---

[32] Data from the NASA Exoplanet Archive, accessed on 2023 October 4 at 11:55, returning 35,086 rows.
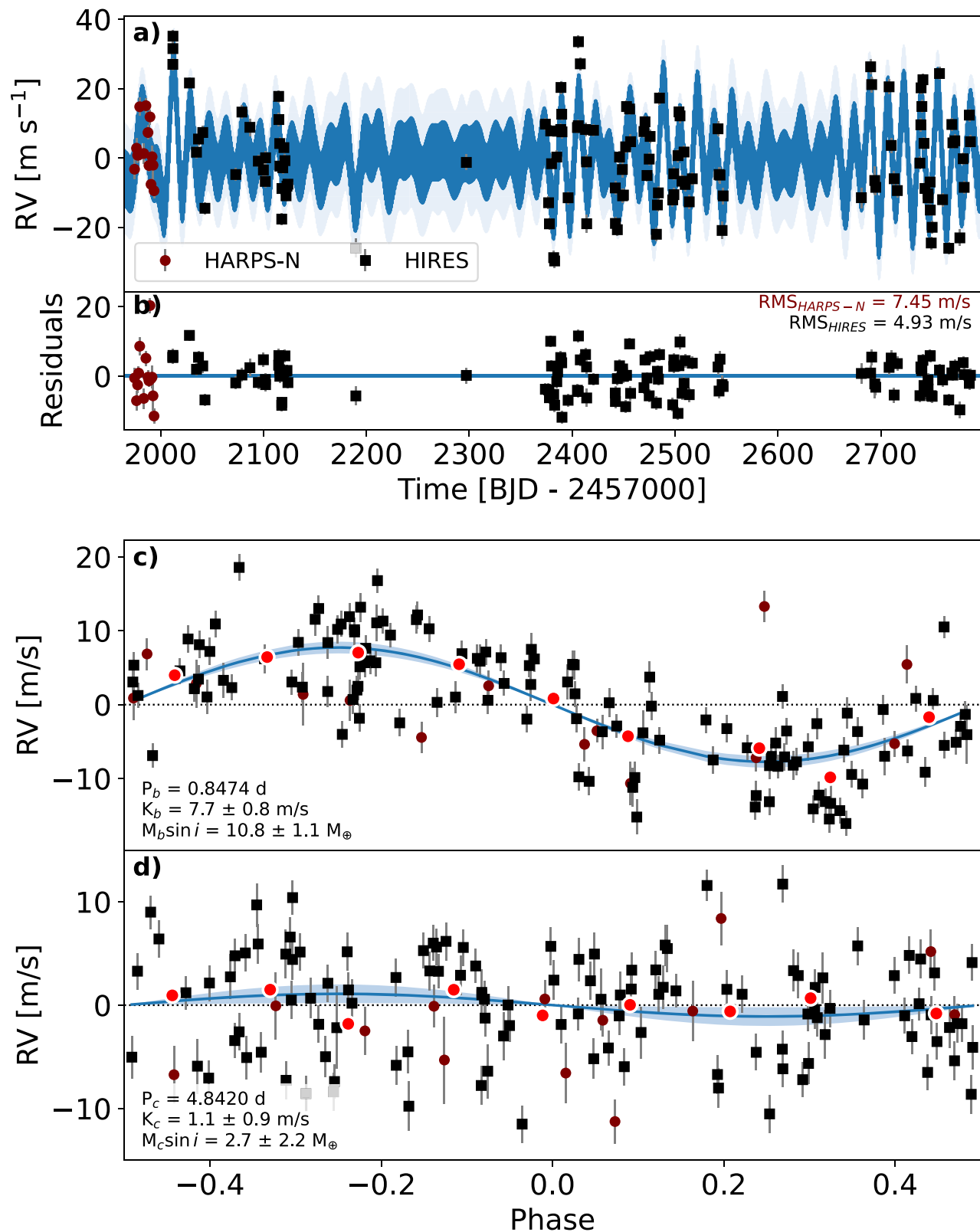
Figure 7. The adopted RV model. Panel (a) shows the HARPS-N and HIRES RV data sets, with the MAP RV model (Keplerian + GP and 1σ uncertainty) overplotted in blue. Panel (b) shows the residuals between the data and the MAP RV model. Panels (c) and (d) show the data phase folded to the orbital period of planets b and c, respectively, with contributions from the other planet and the GP removed. The red points are equal RV bins spanning 0.1 in phase. The median and central 68% credible interval of each Keplerian model is plotted in blue. The MCMC posteriors for the recovered semiamplitude and derived $M \sin i$ are also summarized in the lower left annotations. Note that we do not include the MAP stellar jitter in the plotted error bars; error bars are drawn only as the measurement uncertainties to highlight the degree of unexplained scatter (i.e., jitter), given by the annotated residual rms, to which the stellar jitter fits.
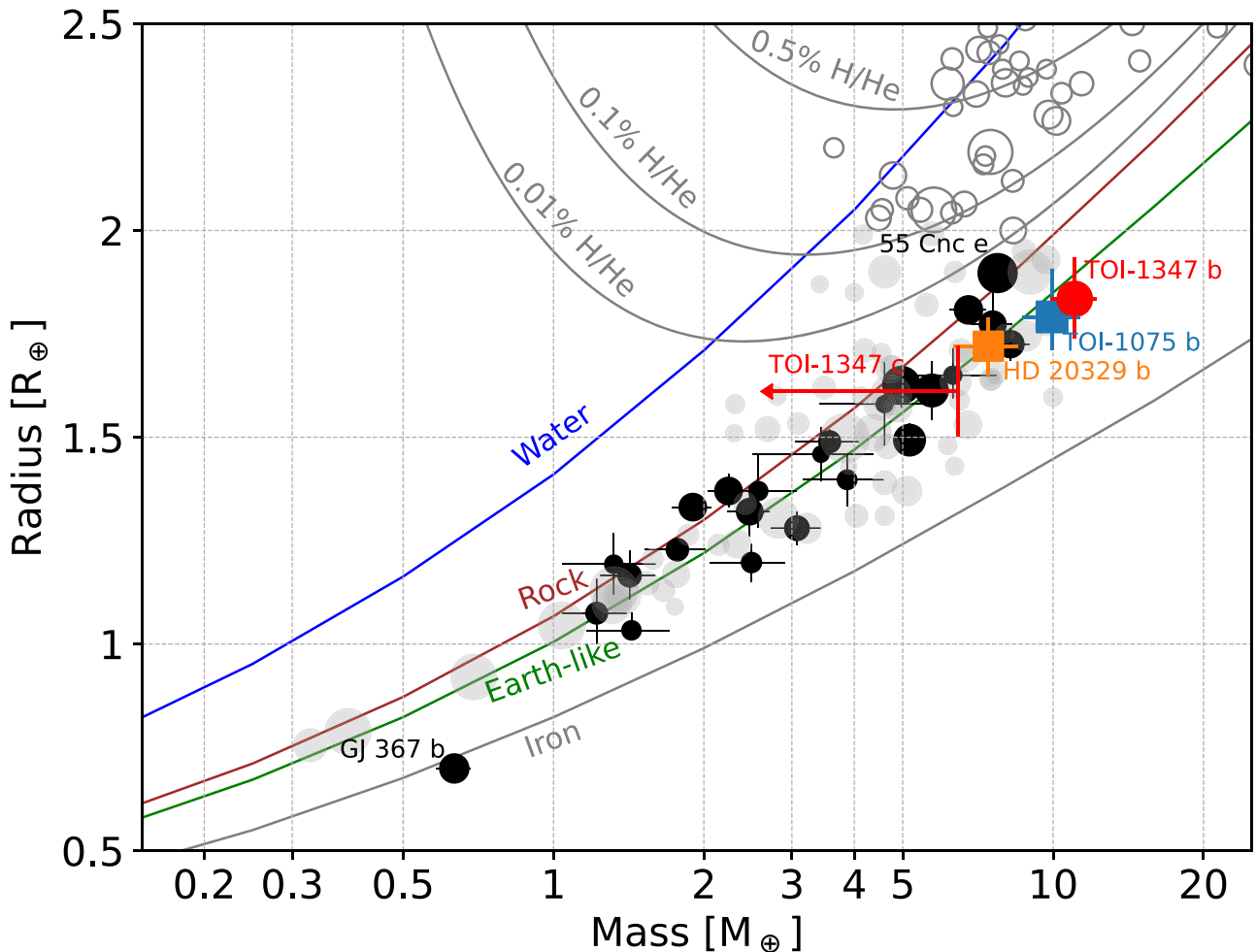
Figure 8. Mass–radius diagram of known super-Earths ($R_p < 2\,R_\oplus$, filled circles) and sub-Neptunes ($4\,R_\oplus > R_p \geqslant 2\,R_\oplus$, empty circles) with 5σ or better mass measurements, obtained from the NASA Exoplanet Archive (NASA Exoplanet Archive 2023). Solid black points denote USPs. Contours from Zeng et al. (2016) are drawn for pure-iron, Earth-like (30% iron, 70% rock), pure-rock, and pure-water compositions. Contours from Chen & Rogers (2016) are also drawn for 0.5%, 0.1%, and 0.01% H/He envelopes surrounding rocky-composition cores, at an age of 1.4 Gyr old and at the maximum insolation flux of 400 $S_\oplus$ for their model grids; it is worth noting that TOI-1347 b (1400 K, $A = 0.7$) receives an insolation flux of around 3000 $S_\oplus$. Our mass–radius constraints for TOI-1347 b and c (95% upper limit in mass) are plotted and labeled in red. The size of each point is proportional to M/σ_M. TOI-1347 b is the most massive super-Earth USP to date, while TOI-1347 c is smaller but likely also rocky.

similar story for TOI-1347 b (TSM =19, ESM =5.6, using the equations of Kempton et al. 2018).

Alternatively, the high-amplitude TESS phase curve of TOI-1347 b may be a consequence of outgassed Na emission on the hot dayside of the planet. Zieba et al. (2022) showed that this emission can explain the phase curve of the lava world K2-141 b, which has been observed in both the Kepler passband and Spitzer-4.5 μm passband (Malavolta et al. 2018). In their analysis, they found that the two phase curves are inconsistent with a blackbody model, with the visible-light phase curve having a higher amplitude than expected. Similarly high visible-light phase-curve amplitudes have been reported for the lava worlds 55 Cnc e (Kipping & Jansen 2020) and Kepler-10 b (Batalha et al. 2011; Rouan et al. 2011) although the latter has not yet been observed in the infrared, which would test blackbody emission. If Na emission is responsible for the observations of TOI-1347 b reported here, it may more easily explain the tentative phase-curve offset than reflective clouds, which would need to be nonuniformly distributed across the planet.

7. Summary

We have characterized two transiting planets in the TOI-1347 system, TOI-1347 b, a USP (0.85 day), and its outer small companion TOI-1347 c (4.84 days). Using TESS photometry and an independent transit fitting pipeline, we measured a radius of $1.8 \pm 0.1\,R_\oplus$ for the USP and $1.6 \pm 0.1\,R_\oplus$ for its companion. We conducted an RV campaign of the TOI-1347 system with HIRES (as part of TKS) and with HARPS-N. We measured a mass of $11.1 \pm 1.2\,M_\oplus$ for the USP, consistent with a bulk Earth-like composition and inconsistent with a H/He envelope (see Figure 8). This composition is perhaps unsurprising given the system age of 1.4 ± 0.4 Gyr, the short timescale on which intensive photoevaporation operates (few hundred megayears), and the high insolation flux at TOI-1347 b's orbit; any primordial H/He envelope should have been destroyed by now. We were unable to detect the companion TOI-1347 c with RVs. We placed a 95% upper limit of $<6.4\,M_\oplus$. Of note is the minimum mutual inclination between planets b and c implied by our measured orbital inclinations: $\sim 7^\circ$. This is unusually large compared to typical

Kepler multis (Fabrycky et al. 2014), which may be another indicator of the migration dynamics that produce USPs.

TOI-1347 b is the most massive of the $<2\,R_\oplus$ (i.e., primarily solid by volume) USPs to date. Its mass sets an upper limit on runaway accretion processes and places TOI-1347 b in a region of the mass–radius diagram in which the pressures and temperatures reached inside the planet have not been well characterized either by experiments or theoretical modeling.

Intriguingly, we measured a tentative (3σ) phase-curve variability, as well as a secondary eclipse (2σ) for the USP TOI-1347 b. The phase curve asymmetry strongly suggests an optically thick atmosphere. However, our mass and radius measurements of TOI-1347 b are highly inconsistent with any significant H/He envelope. As a result, any such atmosphere must have a high-mean molecular weight. It could be comprised of reflective silicate clouds, or may be the result of the outgassing of Na from the molten surface. Future observations (e.g., with JWST) would help confirm such an atmosphere and reveal its composition.

Acknowledgments

Appendix

Here we present the posterior distributions for the full RV model (Figure 9), as well as the table of RV observations analyzed in Section 5 (Table 3).
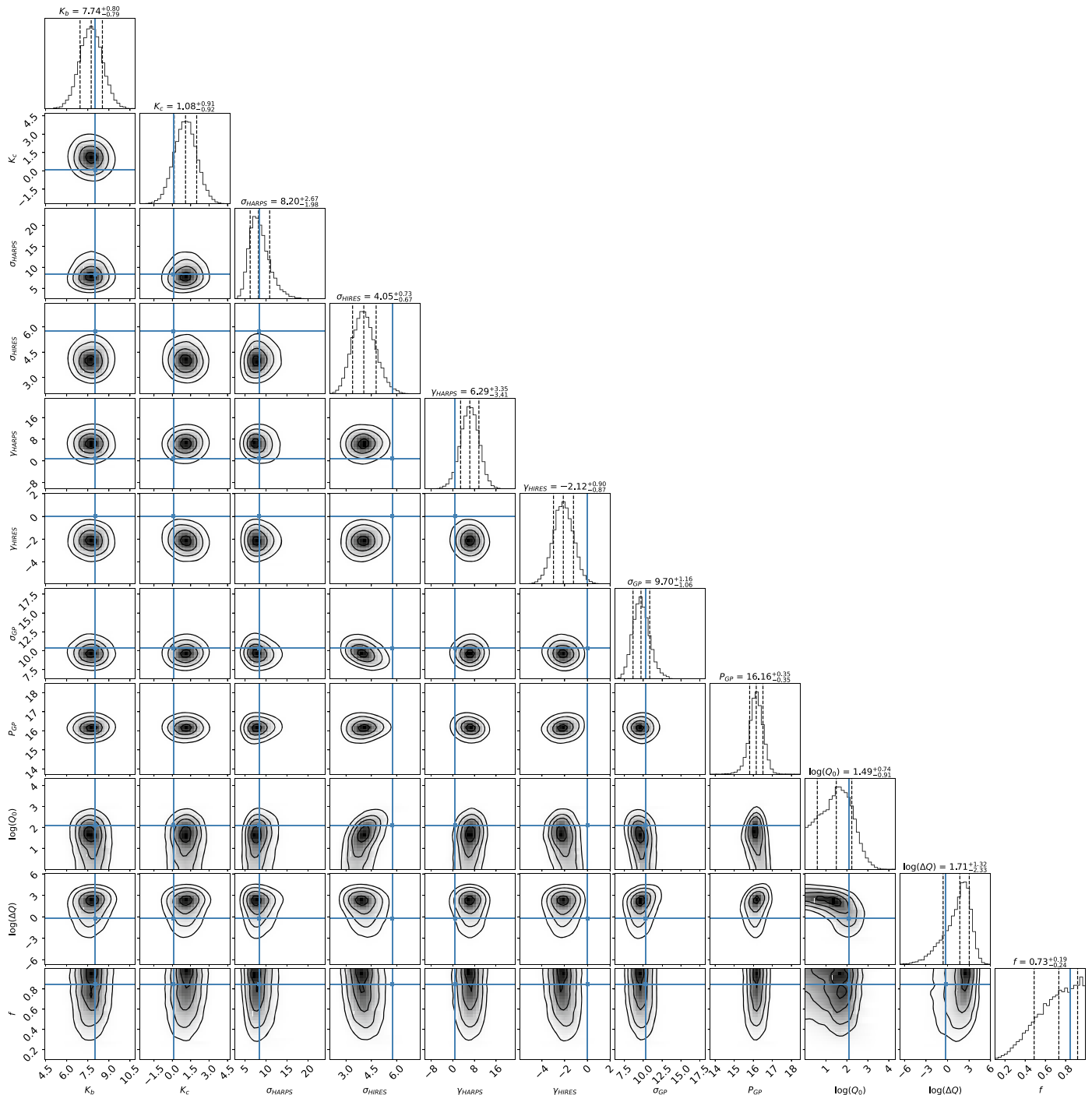

Figure 9. Full posterior distributions for the RV model described in Section 5.1. The blue lines denote the MAP values.

Table 3
TOI-1347 RVs and S-Indices

Time (BJD-2457000)	RV[a] (m s^{-1})	RV Error (m s^{-1})	S_{HK} Index	S_{HK} Index Error	Instrument
2458974.658616	−2.385	2.91	⋯	⋯	HARPS-N
2458976.56778	3.675	2.77	⋯	⋯	HARPS-N
2458977.647243	1.645	2.3	⋯	⋯	HARPS-N
2458978.664451	1.735	1.84	⋯	⋯	HARPS-N
2458979.661071	15.635	2.56	⋯	⋯	HARPS-N
2458983.624618	2.145	2.92	⋯	⋯	HARPS-N
2458985.688595	15.945	2.17	⋯	⋯	HARPS-N
2458987.721405	8.195	2.07	⋯	⋯	HARPS-N
2458988.675995	−1.315	1.57	⋯	⋯	HARPS-N
2458989.689122	12.705	2.12	⋯	⋯	HARPS-N
2458990.665386	−6.745	1.76	⋯	⋯	HARPS-N
2458991.669197	1.215	3.26	⋯	⋯	HARPS-N
2458992.622382	−1.215	4.22	⋯	⋯	HARPS-N
2458993.586943	−8.595	2.12	⋯	⋯	HARPS-N
2459011.871925	27.023	1.73	0.291	0.001	HIRES
2459011.945652	31.576	1.75	0.285	0.001	HIRES
2459011.999298	35.149	1.85	0.287	0.001	HIRES
2459028.000963	21.648	1.49	0.285	0.001	HIRES
2459034.871693	1.685	1.74	0.284	0.001	HIRES
2459036.801673	5.49	1.85	0.281	0.001	HIRES
2459040.959633	7.374	1.88	0.277	0.001	HIRES
2459043.067716	−14.481	1.69	0.278	0.001	HIRES
2459073.019955	−4.758	1.77	0.263	0.001	HIRES
2459079.02133	13.265	1.94	0.271	0.001	HIRES
2459086.759188	8.866	2.45	0.261	0.001	HIRES
2459094.963738	−0.889	1.81	0.256	0.001	HIRES
2459099.906082	−3.443	2.08	0.258	0.001	HIRES
2459101.74781	−6.744	1.72	0.275	0.001	HIRES
2459102.001018	0.082	1.95	0.274	0.001	HIRES
2459114.730454	17.792	1.68	0.277	0.001	HIRES
2459114.919621	11.108	1.97	0.277	0.001	HIRES
2459115.767787	4.19	1.76	0.281	0.001	HIRES
2459115.851596	−2.33	1.81	0.278	0.001	HIRES
2459117.73074	−17.608	1.7	0.276	0.001	HIRES
2459117.892083	−8.786	1.65	0.274	0.001	HIRES
2459118.725156	−2.82	1.71	0.275	0.001	HIRES
2459119.822351	3.015	1.62	0.262	0.001	HIRES
2459120.849961	−0.745	1.84	0.261	0.001	HIRES
2459121.893938	−10.875	1.62	0.263	0.001	HIRES
2459122.813237	−8.108	1.67	0.264	0.001	HIRES
2459123.723648	−7.533	1.58	0.264	0.001	HIRES
2459189.746637	−25.975	2.66	0.279	0.001	HIRES
2459297.143477	−1.254	2.29	0.319	0.001	HIRES
2459373.951805	9.778	1.68	0.306	0.001	HIRES
2459377.047988	−12.886	1.79	0.296	0.001	HIRES
2459377.869358	−18.981	1.72	0.296	0.001	HIRES
2459379.121054	7.817	1.65	0.29	0.001	HIRES
2459379.945803	−1.632	1.65	0.282	0.001	HIRES
2459382.038048	−28.729	2.01	0.268	0.001	HIRES
2459382.957833	−29.687	1.89	0.278	0.001	HIRES
2459385.051386	0.288	1.78	0.285	0.001	HIRES
2459385.877791	7.743	1.73	0.289	0.001	HIRES
2459388.847531	8.234	1.79	0.309	0.001	HIRES
2459389.113887	20.363	1.85	0.313	0.001	HIRES
2459389.840061	12.641	1.64	0.311	0.001	HIRES
2459390.10277	7.56	1.79	0.31	0.001	HIRES
2459396.049221	−11.462	1.87	0.281	0.001	HIRES
2459405.116336	8.808	1.68	0.309	0.001	HIRES
2459405.952026	9.326	1.77	0.315	0.001	HIRES
2459406.101749	33.565	1.79	0.31	0.001	HIRES
2459407.905698	27.179	1.8	0.0	0.001	HIRES

Table 3
(Continued)

Time (BJD-2457000)	RV[a] (m s^{-1})	RV Error (m s^{-1})	S_{HK} Index	S_{HK} Index Error	Instrument
2459413.001295	8.237	1.94	0.284	0.001	HIRES
2459413.964231	−1.111	1.9	0.278	0.001	HIRES
2459414.118005	−18.948	2.63	0.239	0.001	HIRES
2459420.770145	8.008	1.68	0.292	0.001	HIRES
2459441.889385	−8.624	1.95	0.311	0.001	HIRES
2459442.029629	−18.863	1.85	0.305	0.001	HIRES
2459443.913165	−20.67	1.83	0.302	0.001	HIRES
2459446.031598	0.282	1.75	0.283	0.001	HIRES
2459448.761484	−3.308	2.23	0.281	0.001	HIRES
2459449.003801	−10.891	2.09	0.277	0.001	HIRES
2459449.860035	−10.669	1.84	0.278	0.001	HIRES
2459451.981593	3.237	1.83	0.273	0.001	HIRES
2459452.83527	14.859	1.76	0.283	0.001	HIRES
2459455.789937	14.152	1.61	0.303	0.001	HIRES
2459456.77851	4.719	1.99	0.311	0.001	HIRES
2459469.778004	7.652	1.7	0.291	0.001	HIRES
2459470.793047	10.455	1.6	0.299	0.001	HIRES
2459472.733849	−5.021	1.58	0.301	0.001	HIRES
2459474.860635	−0.301	1.87	0.301	0.001	HIRES
2459475.765816	6.237	1.91	0.296	0.001	HIRES
2459481.868763	−21.987	1.88	0.286	0.001	HIRES
2459482.872647	−13.532	1.72	0.285	0.001	HIRES
2459483.768718	−10.044	1.85	0.284	0.001	HIRES
2459484.888563	17.3	1.8	0.294	0.001	HIRES
2459497.736124	−12.074	1.92	0.283	0.001	HIRES
2459498.730087	−4.543	1.77	0.284	0.001	HIRES
2459498.878826	−10.565	1.89	0.286	0.001	HIRES
2459502.866887	0.693	1.82	0.316	0.001	HIRES
2459503.799484	13.319	1.74	0.307	0.001	HIRES
2459504.809106	12.162	2.11	0.316	0.001	HIRES
2459506.714657	−6.684	1.96	0.322	0.001	HIRES
2459508.769583	1.738	1.86	0.31	0.001	HIRES
2459509.853591	−7.617	1.97	0.302	0.001	HIRES
2459513.787074	−12.625	2.06	0.29	0.001	HIRES
2459516.749338	−5.973	1.84	0.288	0.001	HIRES
2459541.764685	8.434	2.21	0.306	0.001	HIRES
2459542.750956	−4.746	2.14	0.31	0.001	HIRES
2459543.709322	−4.926	2.34	0.299	0.001	HIRES
2459545.717882	−20.888	2.51	0.292	0.001	HIRES
2459546.758504	−10.908	2.34	0.292	0.001	HIRES
2459681.066484	−11.429	2.97	0.308	0.001	HIRES
2459690.076369	26.327	2.2	0.326	0.001	HIRES
2459691.125173	21.194	2.28	0.33	0.001	HIRES
2459694.098406	−6.466	3.98	0.338	0.001	HIRES
2459695.041332	−8.45	2.31	0.334	0.001	HIRES
2459708.022865	20.552	2.18	0.336	0.001	HIRES
2459710.08107	3.64	2.11	0.335	0.001	HIRES
2459712.956673	−5.968	2.1	0.308	0.001	HIRES
2459716.048527	−9.38	2.01	0.297	0.001	HIRES
2459738.012297	−1.455	1.86	0.316	0.001	HIRES
2459738.903643	9.585	1.9	0.326	0.001	HIRES
2459739.110148	20.248	1.84	0.337	0.001	HIRES
2459739.881402	14.875	1.83	0.335	0.001	HIRES
2459740.912726	22.59	1.81	0.338	0.001	HIRES
2459741.96611	4.237	1.78	0.328	0.001	HIRES
2459742.920385	−8.773	2.08	0.33	0.001	HIRES
2459745.878305	−10.306	1.83	0.295	0.001	HIRES
2459745.911268	−11.487	1.75	0.301	0.001	HIRES
2459747.905515	−6.925	1.71	0.288	0.001	HIRES
2459748.075272	−15.008	1.75	0.287	0.001	HIRES
2459748.985451	−24.499	1.81	0.286	0.001	HIRES

Time (BJD-2457000)	RV[a] (m s^{-1})	RV Error (m s^{-1})	S_{HK} Index	S_{HK} Index Error	Instrument
2459749.881961	−19.976	1.77	0.283	0.001	HIRES
2459756.993647	24.379	1.78	0.318	0.001	HIRES
2459760.025542	−12.004	1.92	0.313	0.001	HIRES
2459766.003617	−26.032	1.73	0.281	0.001	HIRES
2459769.01945	9.678	1.8	0.286	0.001	HIRES
2459770.019978	4.399	1.58	0.298	0.001	HIRES
2459771.904391	4.986	1.85	0.314	0.001	HIRES
2459776.819221	−23.025	2.38	0.304	0.001	HIRES
2459780.003495	−0.199	1.76	0.293	0.001	HIRES
2459780.996733	−8.457	1.84	0.291	0.001	HIRES
2459785.993673	12.388	1.79	0.292	0.001	HIRES
2459787.063914	4.716	1.84	0.299	0.001	HIRES

Note.
[a] A median value of −13965.395 km s^{-1} has been subtracted from the HARPS-N RVs.

ORCID iDs

Ryan A. Rubenzahl https://orcid.org/0000-0003-3856-3143
Fei Dai https://orcid.org/0000-0002-8958-0683
Andrew W. Howard https://orcid.org/0000-0001-8638-0320
Jack J. Lissauer https://orcid.org/0000-0001-6513-1659
Judah Van Zandt https://orcid.org/0000-0002-4290-6826
Corey Beard https://orcid.org/0000-0001-7708-2364
Steven Giacalone https://orcid.org/0000-0002-8965-3969
Joseph M. Akana Murphy https://orcid.org/0000-0001-8898-8284
Ashley Chontos https://orcid.org/0000-0003-1125-2564
Jack Lubin https://orcid.org/0000-0001-8342-7736
Casey L. Brinkman https://orcid.org/0000-0002-4480-310X
Dakotah Tyler https://orcid.org/0000-0003-0298-4667
Mason G. MacDougall https://orcid.org/0000-0003-2562-9043
Malena Rice https://orcid.org/0000-0002-7670-670X
Paul A. Dalba https://orcid.org/0000-0002-4297-5506
Andrew W. Mayo https://orcid.org/0000-0002-7216-2135
Lauren M. Weiss https://orcid.org/0000-0002-3725-3058
Alex S. Polanski https://orcid.org/0000-0001-7047-8681
Sarah Blunt https://orcid.org/0000-0002-3199-2888
Samuel W. Yee https://orcid.org/0000-0001-7961-3907
Michelle L. Hill https://orcid.org/0000-0002-0139-4756
Isabel Angelo https://orcid.org/0000-0002-9751-2664
Emma V. Turtelboom https://orcid.org/0000-0002-1845-2617
Rae Holcomb https://orcid.org/0000-0002-5034-9476
Aida Behmard https://orcid.org/0000-0003-0012-9093
Daria Pidhorodetska https://orcid.org/0000-0001-9771-7953
Natalie M. Batalha https://orcid.org/0000-0002-7030-9519
Courtney Dressing https://orcid.org/0000-0001-8189-0233
Benjamin Fulton https://orcid.org/0000-0003-3504-5316
Daniel Huber https://orcid.org/0000-0001-8832-4488
Howard Isaacson https://orcid.org/0000-0002-0531-1073
Stephen R. Kane https://orcid.org/0000-0002-7084-0529
Erik A. Petigura https://orcid.org/0000-0003-0967-2893
Paul Robertson https://orcid.org/0000-0003-0149-9678
Nicholas Scarsdale https://orcid.org/0000-0003-3623-7280
Teo Mocnik https://orcid.org/0000-0003-4603-556X
Tara Fetherolf https://orcid.org/0000-0002-3551-279X
Luca Malavolta https://orcid.org/0000-0002-6492-2085
Annelies Mortier https://orcid.org/0000-0001-7254-4363
Aldo Fiorenzano https://orcid.org/0000-0002-4272-4272
Marco Pedani https://orcid.org/0000-0002-5752-6260

References

Aigrain, S., & Foreman-Mackey, D. 2023, ARA&A, 61, 329
Armstrong, D. J., Lopez, T. A., Adibekyan, V., et al. 2020, Natur, 583, 39
Astropy Collaboration, Price-Whelan, A. M., Lim, P. L., et al. 2022, ApJ, 935, 167
Astropy Collaboration, Price-Whelan, A. M., Sipőcz, B. M., et al. 2018, AJ, 156, 123
Astropy Collaboration, Robitaille, T. P., Tollerud, E. J., et al. 2013, A&A, 558, A33
Batalha, N. M., Borucki, W. J., Bryson, S. T., et al. 2011, ApJ, 729, 27
Batygin, K., Stevenson, D. J., & Bodenheimer, P. H. 2011, ApJ, 738, 1
Berger, T. A., Howard, A. W., & Boesgaard, A. M. 2018, ApJ, 855, 115
Berger, T. A., Huber, D., van Saders, J. L., et al. 2020, AJ, 159, 280
Blunt, S., Carvalho, A., David, T. J., et al. 2023, AJ, 166, 62
Borucki, W. J., Koch, D., Basri, G., et al. 2010, Sci, 327, 977
Bouma, L. G., Palumbo, E. K., & Hillenbrand, L. A. 2023, ApJL, 947, L3
Butler, R. P., Marcy, G. W., Williams, E., et al. 1996, PASP, 108, 500
Chachan, Y., Lee, E. J., & Knutson, H. A. 2021, ApJ, 919, 63
Chen, H., & Rogers, L. A. 2016, ApJ, 831, 180
Chontos, A., Murphy, J. M. A., MacDougall, M. G., et al. 2022, AJ, 163, 297
Cosentino, R., Lovis, C., Pepe, F., et al. 2012, Proc. SPIE, 8446, 84461V
Coşkunoğlu, B., Ak, S., Bilir, S., et al. 2011, MNRAS, 412, 1237
Czesla, S., Schröter, S., Schneider, C. P., et al., 2019 PyA: Python astronomy-related packages, Astrophysics Source Code Library, ascl:1906.010
Dai, F., Howard, A. W., Batalha, N. M., et al. 2021, AJ, 162, 62
Dai, F., Masuda, K., Winn, J. N., & Zeng, L. 2019, ApJ, 883, 79
Dawson, R. I., & Fabrycky, D. C. 2010, ApJ, 722, 937
Demory, B.-O., de Wit, J., Lewis, N., et al. 2013, ApJL, 776, L25
Demory, B.-O., Gillon, M., de Wit, J., et al. 2016, Natur, 532, 207
Duane, S., Kennedy, A. D., Pendleton, B. J., & Roweth, D. 1987, PhLB, 195, 216
Dumusque, X., Cretignier, M., Sosnowska, D., et al. 2021, A&A, 648, A103
Duncan, D. K., Vaughan, A. H., Wilson, O. C., et al. 1991, ApJS, 76, 383
Essack, Z., Shporer, A., Burt, J. A., et al. 2023, AJ, 165, 47
Fabrycky, D. C., Lissauer, J. J., Ragozzine, D., et al. 2014, ApJ, 790, 146
Foreman-Mackey, D. 2016, JOSS, 1, 24
Foreman-Mackey, D., Agol, E., Ambikasaran, S., & Angus, R. 2017, AJ, 154, 220
Foreman-Mackey, D., Hogg, D. W., Lang, D., & Goodman, J. 2013, PASP, 125, 306
Foreman-Mackey, D., Luger, R., Agol, E., et al. 2021, JOSS, 6, 3285
Fulton, B. J., & Petigura, E. A. 2018, AJ, 156, 264
Fulton, B. J., Petigura, E. A., Blunt, S., & Sinukoff, E. 2018, PASP, 130, 044504
Fulton, B. J., Petigura, E. A., Howard, A. W., et al. 2017, AJ, 154, 109
Gaia Collaboration, Vallenari, A., Brown, A. G. A., et al. 2023, A&A, 674, A1
Giles, H. A. C., Collier Cameron, A., & Haywood, R. D. 2017, MNRAS, 472, 1618
Ginzburg, S., Schlichting, H. E., & Sari, R. 2018, MNRAS, 476, 759
Grunblatt, S. K., Huber, D., Gaidos, E., et al. 2017, AJ, 154, 254
Guerrero, N. M., Seager, S., Huang, C. X., et al. 2021, ApJS, 254, 39
Gupta, A., & Schlichting, H. E. 2019, MNRAS, 487, 24
Harris, C. R., Millman, K. J., van der Walt, S. J., et al. 2020, Natur, 585, 357
Hastings, W. K. 1970, Biometrika, 57, 97
Haywood, R. D., Collier Cameron, A., Queloz, D., et al. 2014, MNRAS, 443, 2517
Haywood, R. D., Collier Cameron, A., Unruh, Y. C., et al. 2016, MNRAS, 457, 3637
Hedges, C., Angus, R., Barentsen, G., et al. 2020, RNAAS, 4, 220
Hoffman, M., & Gelman, A. 2014, J. Mach. Learn. Res., 15, 1593
Holcomb, R. J., Robertson, P., Hartigan, P., Oelkers, R. J., & Robinson, C. 2022, ApJ, 936, 138
Howard, A. W., Johnson, J. A., Marcy, G. W., et al. 2010, ApJ, 721, 1467

Howell, S. B., Everett, M. E., Sherry, W., Horch, E., & Ciardi, D. R. 2011, AJ, 142, 19

Huber, D., Zinn, J., Bojsen-Hansen, M., et al. 2017, ApJ, 844, 102

Hunter, J. D. 2007, CSE, 9, 90

Isaacson, H., & Fischer, D. 2010, ApJ, 725, 875

Jenkins, J. M., Twicken, J. D., McCauliff, S., et al. 2016, Proc. SPIE, 9913, 99133E

Jenkins, J. S., Díaz, M. R., Kurtovic, N. T., et al. 2020, NatAs, 4, 1148

Kane, S. R., Roettenbacher, R. M., Unterborn, C. T., Foley, B. J., & Hill, M. L. 2020, PSJ, 1, 36

Kempton, E. M. R., Bean, J. L., Louie, D. R., et al. 2018, PASP, 130, 114401

Kipping, D., & Jansen, T. 2020, RNAAS, 4, 170

Kipping, D. M. 2013, MNRAS, 435, 2152

Kovács, G., Zucker, S., & Mazeh, T. 2002, A&A, 391, 369

Kreidberg, L. 2015, PASP, 127, 1161

Kreidberg, L., Koll, D. D. B., Morley, C., et al. 2019, Natur, 573, 87

Lee, E. J. 2019, ApJ, 878, 36

Lightkurve Collaboration, Cardoso, J. V. d. M., Hedges, C., et al., 2018 Lightkurve: Kepler and TESS Time Series Analysis in Python, Astrophysics Source Code Library, ascl:1812.013

Lopez, E. D. 2017, MNRAS, 472, 245

MacDougall, M. G., Petigura, E. A., Gilbert, G. J., et al. 2023, AJ, 166, 33

Malavolta, L., Mayo, A. W., Louden, T., et al. 2018, AJ, 155, 107

Mamajek, E. E., & Hillenbrand, L. A. 2008, ApJ, 687, 1264

MAST 2021, TESS Light Curves - All Sectors, STScI/MAST, doi:10.17909/t9-nmc8-f686

Masuda, K., Petigura, E. A., & Hall, O. J. 2022, MNRAS, 510, 5623

Mazeh, T., Holczer, T., & Faigler, S. 2016, A&A, 589, A75

Metropolis, N., Rosenbluth, A. W., Rosenbluth, M. N., Teller, A. H., & Teller, E. 1953, JChPh, 21, 1087

Millholland, S. C., & Spalding, C. 2020, ApJ, 905, 71

Murgas, F., Nowak, G., Masseron, T., et al. 2022, A&A, 668, A158

Murray-Clay, R. A., Chiang, E. I., & Murray, N. 2009, ApJ, 693, 23

NASA Exoplanet Science Institute 2023, Planetary Systems, Version: 2023-10-04 11:55, IPAC, doi:10.26133/NEA12

Neal, R. M. 2011, Handbook of Markov Chain Monte Carlo (London: Chapman and Hall)

Newville, M., Stensitzki, T., Allen, D. B., & Ingargiola, A., 2014 LMFIT: Non-Linear Least-Square Minimization and Curve-Fitting for Python, v0.8.0, Zenodo, doi:10.5281/zenodo.11813

Owen, J. E., & Wu, Y. 2017, ApJ, 847, 29

Paegert, M., Stassun, K. G., Collins, K. A., et al. 2021, arXiv:2108.04778

Pandas development team, 2020 pandas-dev/pandas: Pandas 1.2.4, v1.2.4, Zenodo, doi:10.5281/zenodo.4681666

Petigura, E. A. 2015, PhD thesis, Univ. California, Berkeley

Rafikov, R. R. 2006, ApJ, 648, 666

Rajpaul, V., Aigrain, S., Osborne, M. A., Reece, S., & Roberts, S. 2015, MNRAS, 452, 2269

Ribas, I., Guinan, E. F., Güdel, M., & Audard, M. 2005, ApJ, 622, 680

Ricker, G. R., Winn, J. N., Vanderspek, R., et al. 2015, JATIS, 1, 014003

Rouan, D., Deeg, H. J., Demangeon, O., et al. 2011, ApJL, 741, L30

Saar, S. H., & Donahue, R. A. 1997, ApJ, 485, 319

Salvatier, J., Wiecki, T. V., & Fonnesbeck, C. 2016, PeerJ Comput. Sci., 2, e.55

Sanchis-Ojeda, R., Rappaport, S., Winn, J. N., et al. 2013, ApJ, 774, 54

Sanchis-Ojeda, R., Rappaport, S., Winn, J. N., et al. 2014, ApJ, 787, 47

Scott, N. J., Howell, S. B., Gnilka, C. L., et al. 2021, FrASS, 8, 138

Seager, S., & Mallén-Ornelas, G. 2003, ApJ, 585, 1038

STScI 2018, TESS Input Catalog and Candidate Target List, STScI/MAST, doi:10.17909/FWDT-2X66

Tayar, J., Claytor, Z. R., Huber, D., & van Saders, J. 2022, ApJ, 927, 31

Tsantaki, M., Andreasen, D., & Teixeira, G. 2020, JOSS, 5, 2048

Tsantaki, M., Andreasen, D. T., Teixeira, G. D. C., et al. 2018, MNRAS, 473, 5066

Tu, L., Johnstone, C. P., Güdel, M., & Lammer, H. 2015, A&A, 577, L3

Vehtari, A., Gelman, A., Simpson, D., Carpenter, B., & Bürkner, P.-C. 2021, BayAn, 16, 667

Virtanen, P., Gommers, R., Oliphant, T. E., et al. 2020, NatMe, 17, 261

Vogt, S. S., Allen, S. L., Bigelow, B. C., et al. 1994, Proc. SPIE, 2198, 362

Wang, L., & Dai, F. 2018, ApJ, 860, 175

Weiss, L. M., Dai, F., Huber, D., et al. 2021, AJ, 161, 56

Weiss, L. M., & Marcy, G. W. 2014, ApJL, 783, L6

Zeng, L., Sasselov, D. D., & Jacobsen, S. B. 2016, ApJ, 819, 127

Zieba, S., Zilinskas, M., Kreidberg, L., et al. 2022, A&A, 664, A79